Chip

Research Article

SENSING

DOI: 10.1016/j.chip.2023.100050

Phonon lasing enhanced mass sensor with zeptogram resolution under ambient conditions

Fei Pan[1,2,†], Kaiyu Cui[1,2,†,*], Yidong Huang[1,2,*], Ziming Chen[1,2], Ning Wu[1,2], Guoren Bai[1,2], Zhilei Huang[1,2], Xue Feng[1,2], Fang Liu[1,2] & Wei Zhang[1,2]

[1]*Department of Electronic Engineering, Tsinghua University, Beijing 100084, China* [2]*Beijing National Research Center for Information Science and Technology (BNRist), Beijing 100084, China*

[†]The authors contributed equally to this work.

E-mails: kaiyucui@tsinghua.edu.cn (Kaiyu Cui), yidonghuang@tsinghua.edu.cn (Yidong Huang)

Cite as: Pan, F. et al. Phonon lasing enhanced mass sensor with zeptogram resolution under ambient conditions. *Chip* **2**, 100050 (2023).
https://doi.org/10.1016/j.chip.2023.100050

Received: 22 November 2022

Accepted: 10 April 2023

Published online: 24 April 2023

High-sensitivity mass sensors under ambient conditions are essential in various fields such as biological research, gas sensing and environmental monitoring. In the current work, a phonon lasing enhanced mass sensor was proposed based on an optomechanical crystal cavity under ambient conditions. The phonon lasing was harnessed to achieve ultra-high resolution since it resulted in an extremely narrow mechanical linewidth (less than 10 kHz). Masses with different weights were deposited on the cavity, it is predicted that the maximum resolution for mass sensing can be 65 ± 19 zg, which approaches the mass order of a protein and an oligonucleotide. This implies the potential application of the proposed method in the biomedical fields such as oligonucleotide drug delivery area and the Human Proteome Project.

Keywords: Mass sensing, Optomechanical crystal cavity, Phonon lasing

INTRODUCTION

Mass spectrometry is a powerful analytical technique which is widely adopted to determine the molecular mass of samples, elemental composition and structural information, making it an indispensable tool in qualitative and quantitative applications including biological research, chemical measurements, astrophysical analysis and environmental monitoring[1-4]. Specifically, mechanical oscillator-based mass sensors are widely utilized for high-sensitivity on-chip mass spectrometry by monitoring the intrinsic mechanical frequency shift $\Delta\omega_{\mathrm{mi}}$ when an additional mass is adsorbed onto the oscillator, as shown Fig. 1**a**[5-13]. Based on the relationship $\Delta m = -2(m_{\mathrm{eff}}/\omega_{\mathrm{mi}})\Delta\omega_{\mathrm{mi}}$, a higher intrinsic vibrational frequency ω_{mi}, smaller effective mass m_{eff}, and smaller intrinsic mechanical frequency shift $\Delta\omega_{\mathrm{mi}}$ could lead to a higher mass resolution Δm_{res}, as shown in Fig. 1**b**. Therefore, cantilever[14-16], nanobeam[6,12], nanotube[17-19], and nanowire[20] oscillators are commonly used, owing to their advantages of relatively small effective mass and high mechanical frequency (in the range of kHz to GHz). Over the past decade, mass resolutions from zeptograms[12,16,21] to yoctograms[9,22] have been achieved employing mechanical oscillator-based structures in a vacuum or cryogenic environment. However, due to the large mechanical dissipation caused by the hydrodynamic force in the ambient environment in which the typical mechanical Q factor is only in the order of tens or hundreds[20,23-25], ultrasensitive mass sensing under ambient conditions has not yet been reported. (When the resonance drift of the mechanical frequency caused by the disturbance of noise is much smaller than the mechanical linewidth, the minimum measurable frequency shift $\Delta\omega_{\mathrm{res}}$ is mainly determined by the linewidth of the resonance). Allan deviation is an important parameter for characterizing the frequency stability and analyzing the sensing resolution, which is commonly the main parameter that limits the mass resolution. In the current experiment, phonon lasing narrowed the linewidth of the mechanical mode, causing mechanical frequency shift to the same order of the Allan deviation. Therefore, the mass shift can be conveniently retrieved by the frequency shift and the minimum measured frequency shift can be used, i.e. the mechanical linewidth, to calculate the minimum measured mass shift, which is the mass resolution in the experiment. It is of great significance to conduct mass sensing studies in ambient conditions since the ambient environment is employed in various applications such as biosensing, gas sensing, environmental monitoring and on-chip fabrication[26-30]. Specifically, the ambient conditions is extremely important in biosensing, since various biological particles can be inactivated in vacuum and low-temperature environment. These biological particles were identified and analyzed using mass detection, as shown in Fig. 1**c**. Among them, the detection of oligonucleotides and proteins require a mass resolution that is as small as zeptograms. For practical applications, detection of serum immunoglobulin (IgM), a type of protein, in the blood and the proportion of its isoforms is very important for analyzing the biological immune system, which requires a mass resolution of 190 kDa at least ($\Delta m_{\mathrm{res}} \sim 3.2 \times 10^{-19}$ g $=$ 320 zg, the quality of the lightest isoform). However, the best mass resolution reported under ambient conditions[30] is at the magnitude of attogram (10^{-18} g), which still cannot meet all the requirements of biological tests. Therefore, the development of ultrahigh-sensitivity sensing techniques remains challenging but is very significant in various fields. It has been predicted that the detection sensitivity of pro-

DOI: 10.1016/j.chip.2023.100050

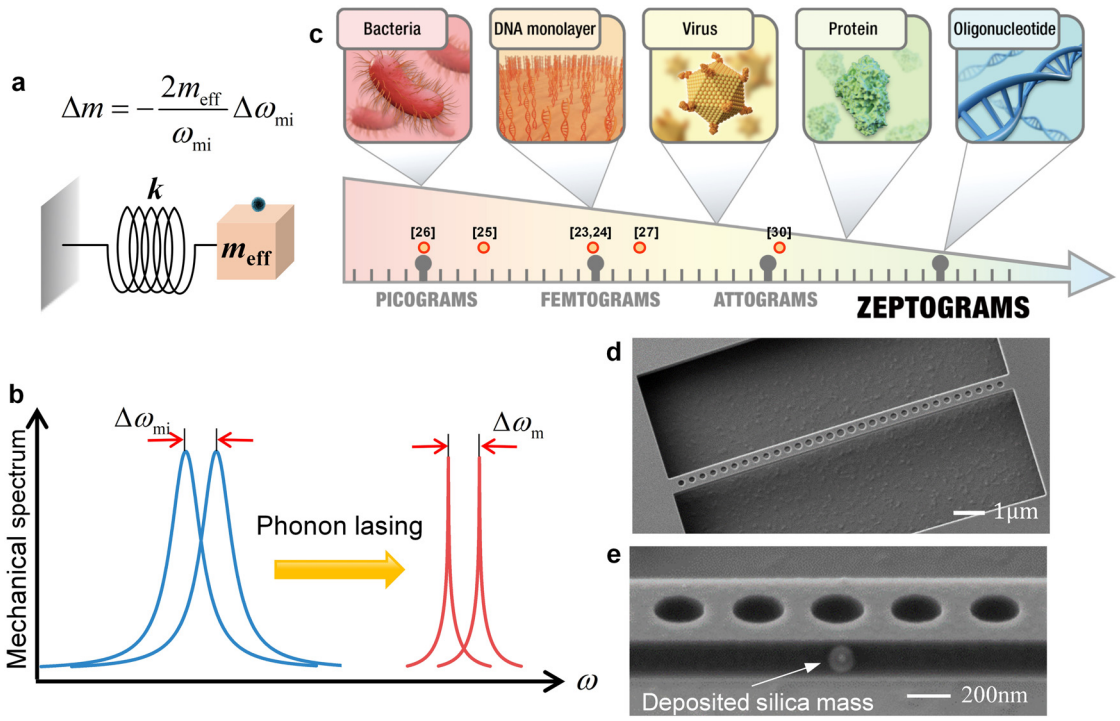

Fig. 1 | Schematic of the proposed optomechanical crystal (OMC) cavity-based mass sensing method. a, Mass sensing mechanism based on mechanical oscillator. **b,** Mechanism of the mass sensing resolution enhancement by phonon lasing resulting from an ultra-narrow mechanical linewidth. **c,** Summary of different bioanalytes[38] and their corresponding masses comparing to the mass sensing resolution of the reported works. **d,** Scanning electron microscope (SEM) image with an oblique view of the designed OMC cavity. **e,** SEM image zoomed on the OMC cavity's sidewall where a silica mass is deposited by the electron beam from a focused ion beam (FIB) system with an oblique view imaging.

tein mass is around 10^{-19} g using optomechanical crystal (OMC) cavity[31], which indicates OMC cavity is possibly applicable for sensitive mass detection. Sub-pg mass sensing has been achieved in microtoroid optomechanical oscillator by the narrow linewidth of phonon lasing combined with harmonic optical modulation[32].

In the current work, a new approach that utilizes phonon lasing to achieve an ultra-narrow mechanical linewidth was proposed, it allows a predicted maximum mass resolution up to zeptograms (10^{-20} g) at room temperature in an ambient environment. The designed sensor structure is a larger-center-hole optomechanical crystal cavity, as shown in Fig. 1**d**, which is referred to as the hole in the center defect region and exhibit a larger radius than that on both sides[33-36]. Its sensing ability was demonstrated by experimentally depositing silica masses of different weights on the OMC cavity, as shown Fig. 1**e**. The results predict that the proposed method allows a maximum resolution of 65 ± 19 zg ($\Delta m_{\mathrm{res}} \sim 6.5 \times 10^{-20}$ g), which approaches the mass of a protein, even an oligonucleotide[37]. This is of great value for possible future applications in biological researches such as oligonucleotide drug delivery[38] or the Human Proteome Project[39].

PHONON LASING NARROWED MECHANICAL LINEWIDTH

Narrower mechanical linewidth could lead to higher mass resolution, as shown in Fig. 1**a**. In this study, a mass sensing that was phonon lasing enhanced was proposed, which dramatically causes the narrowing of the mechanical linewidth[40]. Here, the optical gradient force generated by the radiation pressure was utilized to measure and amplify the mechanical mode. In this process, the blue detuned pump light is scattered to lower frequency due to the mechanical motion, providing energy to the mechanical system. It is an effective gain to the mechanical system and will compensate for the energy loss from the other damping channels. In addition, since the compensation for the mechanical dissipation provided by the optical gradient force is proportional to the photon number in the OMC cavity, a high optical Q factor is required to be taken into consideration when designing the OMC cavity to achieve a higher optical gradient force and favor the phonon lasing. Moreover, OMC cavities with lower intrinsic mechanical dissipation are beneficial for phonon lasing. Therefore, in the current work, the larger-center-hole OMC cavity shown in Figs. 1**d** and 2**a**, which was proposed in our previous study[33-36], was selected due to its high optical Q factor and low intrinsic mechanical dissipation for the phonon lasing enhanced mass sensor.

The OMC cavity was designed and optimized using the finite element method (FEM). Here, a localized optical fundamental mode (i.e., y-component of the normalized electric field E_y) with a wavelength of 1546.8 nm, as shown in Fig. 2**b**, and a localized mechanical fundamental mode with a mechanical frequency of 4.43 GHz, as shown in Fig. 2**c**, were formed in the cavity through the optical and mechanical bandgaps, respectively. In addition, by using the definition of effective mass in reference[41], the calculated effective mass for the designed structure was 133 fg. Fig. 2**d** shows the measurements adopting the experimental setup (details for the structural design, fabrication, and measurements in could be seen in Supplementary Notes 1-2). The fundamental optical mode ($\lambda = 1557.6$ nm) is observed in the transmission spectrum, as shown in Fig. 2**e**. As shown in the inset of Fig. 2**e**, the intrinsic optical Q factor was estimated to be 160,000 based on the Lorentzian fitting of the fundamental optical mode. Moreover, results show that the localized mechanical fundamental mode exhibited a relatively narrow linewidth of approximately 3 MHz (Q~1,500) under ambient conditions with a high frequency of 4.526 GHz, as shown in Fig. 3**b** (gray data points). Therefore, the designed structure

DOI: 10.1016/j.chip.2023.100050

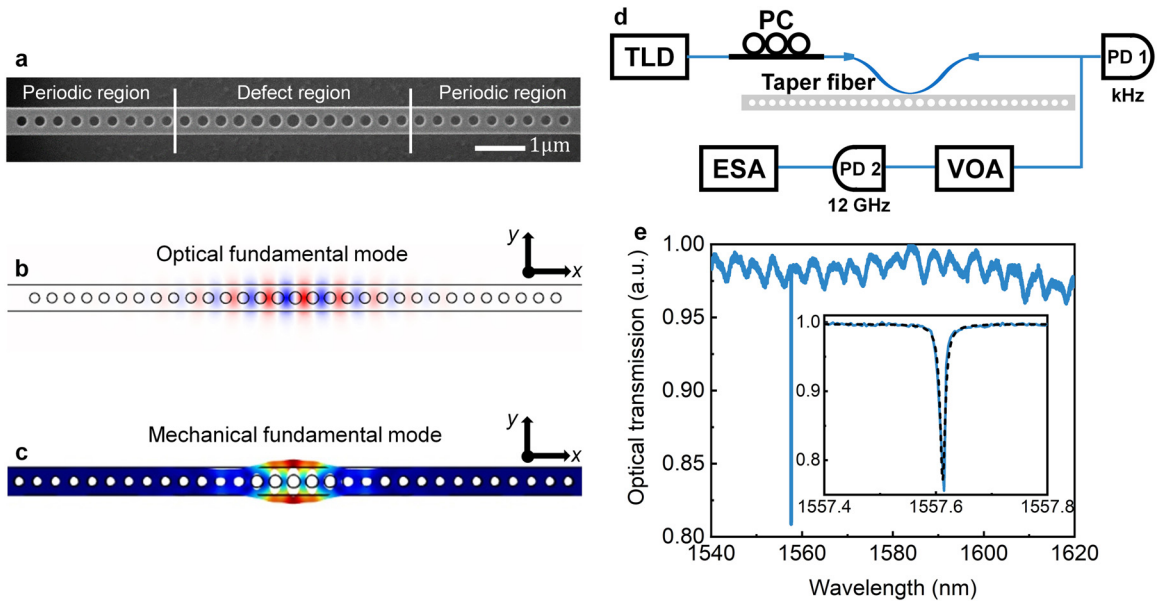

Fig. 2 | Characterization of the designed OMC cavity. a, SEM image with top view of the cavity. It consists of three parts: one defect region between two identical periodic mirror regions. **b,** Normalized electric y-component (E_y) of the localized optical fundamental mode with a wavelength of 1546.8 nm. **c,** Normalized displacement field of the confined fundamental mechanical mode with a frequency of 4.43 GHz. Both the optical and mechanical modes were calculated using the finite element method (FEM). **d,** A tunable laser diode (TDL), polarization controller (PC) and photodetector with a bandwidth of approximately kilohertz (PD1), photodetector with a bandwidth of 12 GHz (PD2), viable optical attenuator (VOA), and electrical spectrum analyzer (ESA) constitute the experimental setup. The electronic spectrums were averaged 8 times, and the resolution bandwidth was set as 0.51MHz (510Hz) before (after) the phonon lasing during the experiment. **e,** Optical transmission spectrum shows the fundamental mode centered at 1557.6 nm with an intrinsic Q factor of 160,000 (in the inset).

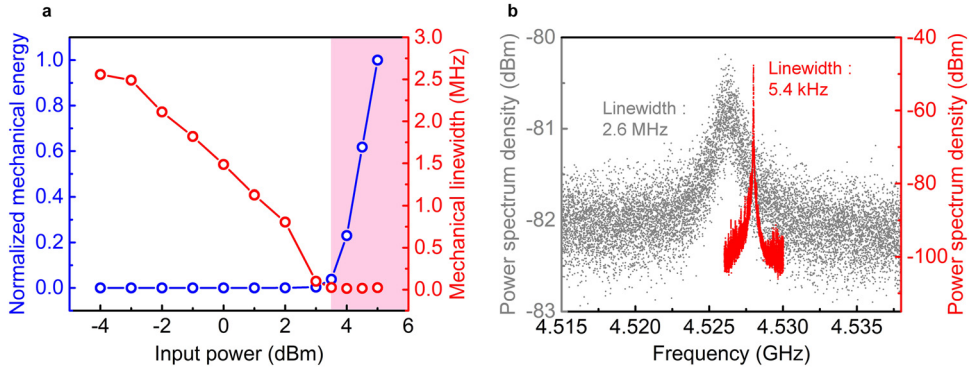

Fig. 3 | Measurement of phonon lasing. a, Normalized mechanical energy and linewidth versus the pump laser power (input power). The mechanical linewidth is narrowed from 2.6 MHz to 5.4 kHz after phonon lasing (pink shaded area). The minimum linewidth is associated with the input power. **b,** Power spectrum density (PDS) for the fundamental mechanical mode is measured at room temperature under atmospheric conditions with a low input laser power of −4 dBm, and the mechanical frequency and linewidth is 4.526 GHz and 2.6 MHz (gray data points), respectively. The red data points are the PDS after phonon lasing with an extremely narrowed linewidth of 5.4 kHz that was measured at a high input laser power of 5 dBm.

is of high optical intrinsic Q factors and low intrinsic mechanical property to favor phonon lasing under ambient conditions.

Phonon lasing was experimentally achieved in the OMC cavity by increasing the optical input power to amplify the Stokes scattering process, as shown in Fig. 3. The wavelength of the input laser (TLD) shown in Fig. 2**d** was adjusted in the blue-detuned regime. The detuning Δ is defined as $\Delta = \omega_{in} - \omega_o$, where, ω_{in} and ω_o depict the frequencies of the input laser and the cavity resonance, respectively. An apparent threshold shown in Fig. 3**a** was found to be the optical input power increased along a narrowed mechanical linewidth after reaching the threshold, indicating that phonon lasing was achieved in the fabricated OMC cavity. Subsequently, the mechanical linewidth can be narrowed up to three orders of magnitude, ranging from 2.6 MHz to 5.4 kHz, to realize ultrasensitive mass sensing under ambient conditions, as shown in Fig. 3**b**.

PHONON LASING ENHANCED MASS SENSING

In this section, the experiment to verify a phonon lasing enhanced mass sensing was discussed. The experimental scheme based on the sensing principle $\Delta m = -2(m_{eff}/\omega_{mi})\Delta\omega_{mi}$ is as follows: Firstly, a focused ion beam (FIB) was used to deposit a small amount of material (silica) on the side wall of the OMC cavity via ion beam induced deposition, as shown in Fig. 1**e** (details can be seen in Supplementary Notes 3), resulting in the mechanical frequency shift $\Delta\omega_m$. The deposition parameters were ad-

DOI: 10.1016/j.chip.2023.100050

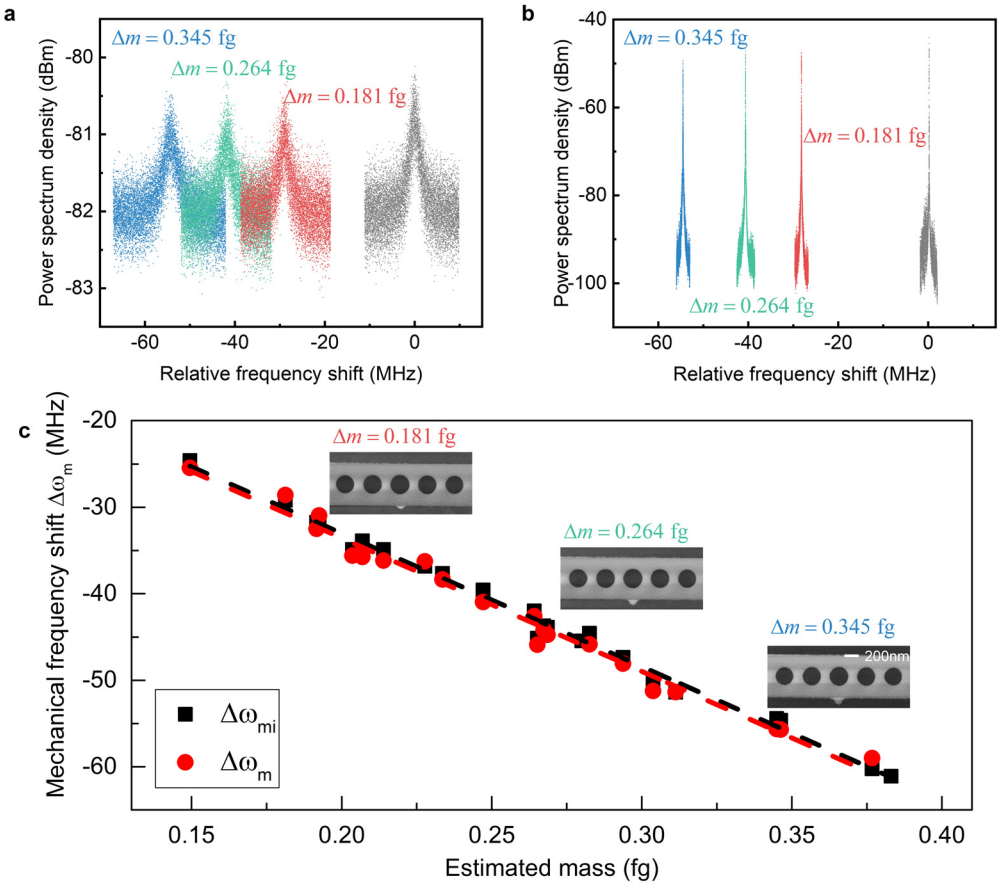

Fig. 4 | Experimental results. a, b, Experimentally measured ω_m on the condition that laser-cavity detuning is sufficiently large and is in phonon lasing regions, respectively. Gray data points are the references to show the mechanical frequency shift caused by the added masses, and the red, green, and blue points show those obtained after the deposition of different weights. The linewidths are 2.7, 3.1, 3.5, and 4.2 MHz from right to left, in **a**, which correspond to a mass of 0.181, 0.264, and 0.345 fg, respectively. The linewidths are narrowed to 3.6, 6.3, 7.6, and 10 kHz, under phonon lasing in **b**, after phonon lasing. It is obvious that the linewidth can hold to 4.2 MHz and can be further narrowed to below 10 kHz, which shows a considerably improved resolvable linewidth that benefits the ultra-sensitive mass sensing method. **c,** Responsivity between the added masses and mechanical frequency shift. The series of the black blocks and red circles are the measured mechanical frequency shift under different deposited weights. Specifically, the black blocks and red circles correspond to the $\Delta\omega_m$, which is measured on the same condition with Fig. 4a ($\Delta\omega_{mi}$) and Fig. 4b ($\Delta\omega_m$), respectively. The slopes ($\Re = \Delta\omega/\Delta m$) of the linear fit are -154 MHz fg^{-1} and -154.1 MHz fg^{-1}, and show a good agreement with each other, which means $\Delta\omega_m \approx \Delta\omega_{mi}$ in the proposed sensing scheme. Therefore, a minimum detectable mass of $\Delta m_{res} \sim 65$ zg $= 6.5 \times 10^{-20}$ g is predicted with the after-deposited 3 dB resolvable linewidth (shown in Fig. 4b).

justed to control the weights of the added masses. Finally, masses of different weights were obtained for mass sensing in the experiments. The limitation and repeatability of the mass deposition process using FIB were further discussed in Supplementary Note 3.

The intrinsic mechanical frequency shift $\Delta\omega_{mi}$ caused by mass deposition was measured firstly, and then the corresponding $\Delta\omega_m$ was measured under phonon lasing to illustrate the experimental results of the enhancement of the sensing resolution. Fig. 4a shows the intrinsic mechanical variation modes for three different deposition parameters. The gray data points represent the measured ω_{mi} prior to mass deposition, which are used as references when exhibiting the mechanical frequency shift corresponding to the added masses. Meanwhile, the red, green, and blue data points represent the measured mechanical vibration modes after depositing different weights of SiO_2 masses, whicl leads to frequency shifts of 29.2, 41.97 and 54.44 MHz, respectively. The homologous masses evaluated by the sensing principle (see details regarding the calculation method of the deposited mass in Supplementary Note 4) are 0.181, 0.264 and 0.345 fg, respectively, corresponding to the insets in Fig. 4c with the same color. Based on the figure, it is apparent that a greater weight could cause a larger mechanical frequency shift, which agrees well with the theoretical analysis in the current work.

Then, the phonon lasing amplification mechanical vibration was measured accordingly, as shown in Fig. 4b with the same color. The mechanical linewidth was narrowed from MHz to kHz, which is favourable to the proposed ultra-sensitive mass sensing method. The measured mechanical frequency ω_m consists of the intrinsic mechanical frequency ω_{mi} and the mechanical frequency deviation ω_{md} induced by the optical spring effect $\omega_m = \omega_{mi} + \omega_{md}$. The responsivities $\Re = \Delta\omega/\Delta m$ were measured under the intrinsic and phonon lasing conditions of the designed OMC cavity so as to experimentally evaluate the influence of the optical spring effect, as shown in Fig. 4c. The black and red circles represent the measured mechanical frequency shift $\Delta\omega_m$ under the condition that the input laser is far away from the cavity resonance (intrinsic mechanical vibration) and after phonon lasing for different deposited masses, respectively. The black and red dashed lines correspond to the linear fittings with responsivities of -154.0 and -154.1 MHz fg^{-1}, wherein the negative sign indicates a decreasing mechanical frequency when the mass is deposited on the cavity. These two sets of data are consistent with each other and demonstrate

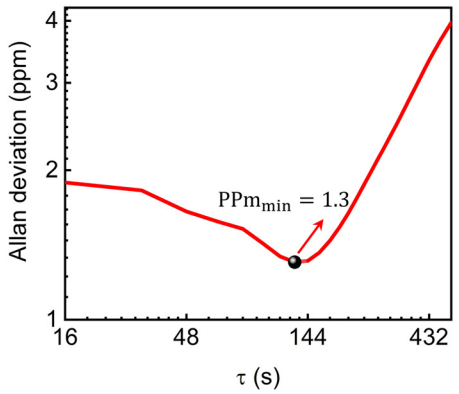

Fig. 5 | Allan deviation of the fundamental mechanical mode, measured under the phonon lasing at ambient conditions shows a minimum deviation of 5.8 kHz, which results in an ultrasmall resolution uncertainty of 38 zg.

that the optical spring effect-induced mechanical frequency deviation ω_{md} can be neglected in the proposed phonon lasing enhanced mass sensing approach in the OMC cavity. Therefore, the deposition-induced mechanical frequency shift under phonon lasing is approximately equal to the intrinsic mechanical frequency shift (i.e. $\Delta\omega_m \approx \Delta\omega_{mi}$) and can be used to directly determine the mass of the added mass Δm. It is found that the optical spring effect-induced mechanical frequency deviation ω_{md} can be neglected in the proposed sensing approach (see the detailed theoretical analysis in Supplementary Notes 5), in which the calculated optical spring-induced frequency deviation was no more than 3% relative to the deposited mass-induced frequency shift.

DISCUSSION

Finally, the sensing resolution was analyzed. The mechanical linewidth is narrowed from 4.2 MHz to its phonon lasing value of approximately 5 kHz by applying Lorentzian fitting to the spectra, as shown in Fig. 4a and Fig. 4b, respectively. It is evident that the experimentally resolvable frequency shift can be significantly improved after phonon lasing, and the mechanical linewidth can be narrowed to approximately 10 kHz even after deposition. The minimum detectable mass is predicted to be $\Delta m_{res} = \Delta\omega_{res}/\Re \sim 65\ \text{zg} = 6.5 \times 10^{-20}$ g based on the responsivity $\Re$ and 3 dB resolvable linewidth $\Delta\omega_{res}$. This high-resolution is an order of magnitude higher than those estimated using the reported routine approaches with Allan deviation[30].

Furthermore, the Allan deviation[42] is also used for the characterization of the frequency stability and analysis of the sensing resolution uncertainty (see details in Supplementary Note 6) in the current work. The Allan deviation of the fundamental mechanical mode after phonon lasing is shown in Fig. 5 with a minimum deviation of 5.8 kHz, which allows for a resolution uncertainty of 38 zg. With this, the resolution of the proposed phonon lasing enhanced ultra-high-sensitive mass sensing in the order of tens of zeptograms is possible for practical applications, which sheds light on on-chip mass sensing components.

CONCLUSIONS

In this study, a phonon lasing enhanced ultra-high-sensitivity mass sensing system was put forward, which describes the direct relationship between the measured mechanical frequency shift $\Delta\omega_m$ and the added mass Δm under ambient conditions. The validity of the method adopted in the current work was experimentally verified by depositing masses with different weights on the cavity and measuring the corresponding sensing responsivity of the cavity in the range of intrinsic mechanical vibration and phonon lasing. Moreover, the mechanical frequency deviation caused by the optical spring effect can be neglected due to the fact that the measured mechanical frequency shifts $\Delta\omega_{mi}$ and $\Delta\omega_m$ coincides well with each other (i.e. $\Delta\omega_m \approx \Delta\omega_{mi}$). In addition, the mechanical linewidth was narrowed to 10 kHz even after the deposition, and the measured Allan deviation showed a frequency stability of 5.8 kHz, thereby indicating a predicted minimum detected mass of $\Delta m_{res} \sim 65 \pm 19$ zg in the experiment. This high resolution shows the potential application of the ultra-sensitive mass sensing in various fields such as biological research, gas sensing and environmental monitoring under ambient conditions.

However, one of the key limits of the proposed mass sensing method with utilizing OMC cavities is that the mechanical mode is extremely localized and the sensitivity is exquisitely dependent on the landing locations of the nanoparticles. This limit may be solved by detecting the mechanical frequency change of multi-modes[31,43,44] in the OMC cavities, which also show different mode distributions with various responses for the landing locations, thus making it possible for position detection[45]. Another limit of this study is that the deposited mass is not calibrated experimentally in the current work, and a parallel time-of-flight mass spectrometer may be employed in the further experiments for this purpose[7]. Another sensing limit of the method with using phonon lasing of the OMC cavities is that it is difficult to be used in the liquid sensing where the phonon lasing is difficult to be achieved. What's more, the Allan deviation can be further improved to decrease the uncertainty of the sensing in the work by introducing multimode phonon lasing[46].

METHODS

The optomechanical cavity in the current work is a larger-center-hole OMC cavity. The periodic unit cell of OMC exhibits the width of 550 nm, lattice constant of 365 nm, the height of 220 nm and diameter of center hole of d_0= 204 nm. In the defect unit cells, the diameters of center holes vary with $d_i = d_0 + i(d_7 - d_0)/7,\ i = 0,\ 1,\ \ldots,\ 7$ and $d_7 = 256.5$ nm. The designed structure was fabricated on a 220 nm thick silicon-on-insulator (SOI) wafer with a 3 μm buried oxide layer. The pattern was defined using the electron beam lithography (EBL) and transferred to the 220 nm silicon layer by inductively coupled plasma (ICP) etching. A buffered hydrofluoric acid (HF) solution was adopted for wet etching to remove the buried oxide layer beneath the nanobeam and release it for further measurements. In the experiment of mass sensing, the silica for mass sensing was deposited by focused ion beam (FIB).

REFERENCES

1. Keifer, D. Z. & Jarrold, M. F. Single-molecule mass spectrometry. *Int. J. Mass Spectrom.* **36**, 715–733 (2017). https://doi.org/10.1002/mas.21495.
2. Doerr, A., Finkelstein, J., Jarchum, I., Goodman, C. & Dekker, B. Nature milestones: mass spectrometry. *Nat. Methods* **12**, 1–46 (2015). https://doi.org/10.1038/nmeth.3558.
3. Mouro, J., Pinto, R., Paoletti, P. & Tiribilli, B. Microcantilever: dynamical response for mass sensing and fluid characterization. *Sensors* **21**, 115 (2020). https://doi.org/10.3390/s21010115.
4. Erdogan, R. T. et al. Atmospheric pressure mass spectrometry of single viruses and nanoparticles by nanoelectromechanical systems. *ACS Nano* **16**, 3821–3833 (2022). https://doi.org/10.1021/acsnano.1c08423.
5. Sansa, M. et al. Optomechanical mass spectrometry. *Nat. Commun.* **11**, 3781 (2020). https://doi.org/10.1038/s41467-020-17592-9.
6. Sage, E. et al. Single-particle mass spectrometry with arrays of frequency-addressed nanomechanical resonators. *Nat. Commun.* **9**, 3283 (2018). https://doi.org/10.1038/s41467-018-05783-4.
7. Sage, E. et al. Neutral particle mass spectrometry with nanomechanical systems. *Nat. Commun.* **6**, 6482 (2015). https://doi.org/10.1038/ncomms7482.

8. Hanay, M. S. et al. Single-protein nanomechanical mass spectrometry in real time. *Nat. Nanotechnol.* **7**, 602–608 (2012). https://doi.org/10.1038/nnano.2012.119.
9. Chaste, J. et al. A nanomechanical mass sensor with yoctogram resolution. *Nat. Nanotechnol.* **7**, 301–304 (2012). https://doi.org/10.1038/nnano.2012.42.
10. Arlett, J. L., Myers, E. B. & Roukes, M. L. Comparative advantages of mechanical biosensors. *Nat. Nanotechnol.* **6**, 203–215 (2011). https://doi.org/10.1038/nnano.2011.44.
11. Boisen, A. Mass spec goes nanomechanical. *Nat. Nanotechnol.* **4**, 404–405 (2009). https://doi.org/10.1038/nnano.2009.169.
12. Yang, Y. T., Callegari, C., Feng, X. L., Ekinci, K. L. & Roukes, M. L. Zeptogram-scale nanomechanical mass sensing. *Nano Lett.* **6**, 583–586 (2006). https://doi.org/10.1021/nl052134m.
13. Pastina, A. D. & Villanueva, L. G. Suspended micro/nano channel resonators: a review. *J. Micromech. Microeng.* **30**, 043001 (2020). https://doi.org/10.1088/1361-6439/ab6df1.
14. Malvar, O. et al. Mass and stiffness spectrometry of nanoparticles and whole intact bacteria by multimode nanomechanical resonators. *Nat. Commun.* **7**, 13452 (2016). https://doi.org/10.1038/ncomms13452.
15. Dohn, S., Schmid, S., Amiot, F. & Boisen, A. Position and mass determination of multiple particles using cantilever based mass sensors. *Appl. Phys. Lett.* **97**, 044103 (2010). https://doi.org/10.1063/1.3473761.
16. Jensen, K., Kim, K. & Zettl, A. An atomic-resolution nanomechanical mass sensor. *Nat. Nanotechnol.* **3**, 533–537 (2008). https://doi.org/10.1038/nnano.2008.200.
17. Lassagne, B., Garcia-Sanchez, D., Aguasca, A. & Bachtold, A. Ultrasensitive mass sensing with a nanotube electromechanical resonator. *Nano Lett.* **8**, 3735–3738 (2008). https://doi.org/10.1021/nl801982v.
18. Chiu, H.-Y., Hung, P., Postma, H. W. C. & Bockrath, M. Atomic-scale mass sensing using carbon nanotube resonators. *Nano Lett.* **8**, 4342–4346 (2008). https://doi.org/10.1021/nl802181c.
19. Gruber, G. et al. Mass sensing for the advanced fabrication of nanomechanical resonators. *Nano Lett.* **19**, 6987–6992 (2019). https://doi.org/10.1021/acs.nanolett.9b02351.
20. Gil-Santos, E. et al. Nanomechanical mass sensing and stiffness spectrometry based on two-dimensional vibrations of resonant nanowires. *Nat. Nanotechnol.* **5**, 641–645 (2010). https://doi.org/10.1038/nnano.2010.151.
21. Nishio, M., Sawaya, S., Akita, S. & Nakayama, Y. Carbon nanotube oscillators toward zeptogram detection. *Appl. Phys. Lett.* **86**, 133111 (2005). https://doi.org/10.1063/1.1896426.
22. Parmar, M. M., Gangavarapu, P. R. Y. & Naik, A. K. Dynamic range tuning of graphene nanoresonators. *Appl. Phys. Lett.* **107**, 113108 (2015). https://doi.org/10.1063/1.4931118.
23. Johnson, L., Gupta, A. K., Ghafoor, A., Akin, D. & Bashir, R. Characterization of vaccinia virus particles using microscale silicon cantilever resonators and atomic force microscopy. *Sens. Actuators B: Chem.* **115**, 189–197 (2006). https://doi.org/10.1016/j.snb.2005.08.047.
24. Cagliani, A., Kosaka, P., Tamayo, J. & Davis, Z. J. Monitoring the hydration of DNA self-assembled monolayers using an extensional nanomechanical resonator. *Lab Chip* **12**, 2069–2073 (2012). https://doi.org/10.1039/C2LC40047B.
25. Ilic, B. et al. Single cell detection with micromechanical oscillators. *J. Vac. Sci. Technol. B* **19**, 2825–2828 (2001). https://doi.org/10.1116/1.1421572.
26. Campanella, H. et al. Localized-mass detection based on thin-film bulk acoustic wave resonators (FBAR): Area and mass location aspects. *Sens. Actuators A: Phys.* **142**, 322–328 (2008). https://doi.org/10.1016/j.sna.2007.05.004.
27. Schmid, S., Kurek, M., Adolphsen, J. Q. & Boisen, A. Real-time single airborne nanoparticle detection with nanomechanical resonant filter-fiber. *Sci. Rep.* **3**, 1288 (2013). https://doi.org/10.1038/srep01288.
28. Soysal, U. et al. Aerosol mass concentration measurements: recent advancements of real-time nano/micro systems. *J. Aerosol. Sci.* **114**, 42–54 (2017). https://doi.org/10.1016/j.jaerosci.2017.09.008.
29. Tamayo, J., Kosaka, P. M., Ruz, J. J., Paulo, Á. S. & Calleja, M. Biosensors based on nanomechanical systems. *Chem. Soc. Rev.* **42**, 1287–1311 (2013). https://doi.org/10.1039/C2CS35293A.
30. Li, M., Tang, H. X. & Roukes, M. L. Ultra-sensitive NEMS-based cantilevers for sensing, scanned probe and very high-frequency applications. *Nat. Nanotechnol.* **2**, 114–120 (2007). https://doi.org/10.1038/nnano.2006.208.
31. Eichenfield, M., Chan, J., Camacho, R. M., Vahala, K. J. & Painter, O. Optomechanical crystals. *Nature* **462**, 78–82 (2009). https://doi.org/10.1038/nature08524.
32. Liu, F., Alaie, S., Leseman, Z. C. & Hossein-Zadeh, M. Sub-pg mass sensing and measurement with an optomechanical oscillator. *Opt. Express* **21**, 19555–19567 (2013). https://doi.org/10.1364/OE.21.019555.
33. Li, Y. et al. Optomechanical crystal nanobeam cavity with high optomechanical coupling rate. *J. Opt.* **17**, 045001 (2015). https://doi.org/10.1088/2040-8978/17/4/045001.
34. Huang, Z. et al. High-mechanical-frequency characteristics of optomechanical crystal cavity with coupling waveguide. *Sci. Rep.* **6**, 34160 (2016). https://doi.org/10.1038/srep34160.
35. Pan, F. et al. Radiation-pressure-antidamping enhanced optomechanical spring sensing. *ACS Photonics* **5**, 4164–4169 (2018). https://doi.org/10.1021/acsphotonics.8b00968.
36. Xu, Q. et al. Tunable mechanical-mode coupling based on nanobeam-double optomechanical cavities. *Photonics Res.* **10**, 1819–1827 (2022). https://doi.org/10.1364/prj.447711.
37. Calleja, M., Kosaka, P. M., Paulo, Á. S. & Tamayo, J. Challenges for nanomechanical sensors in biological detection. *Nanoscale* **4**, 4925–4938 (2012). https://doi.org/10.1039/C2NR31102J.
38. Roberts, T. C., Langer, R. & Wood, M. J. A. Advances in oligonucleotide drug delivery. *Nat. Rev. Drug Discov.* **19**, 673–694 (2020). https://doi.org/10.1038/s41573-020-0075-7.
39. Adhikari, S. et al. A high-stringency blueprint of the human proteome. *Nat. Commun.* **11**, 5301 (2020). https://doi.org/10.1038/s41467-020-19045-9.
40. Xiong, J. et al. Phonon and photon lasing dynamics in optomechanical cavities. *Fundam. Res.* **3**, 37–44 (2023). https://doi.org/10.1016/j.fmre.2022.10.008.
41. Aspelmeyer, M., Kippenberg, T. J. & Marquardt, F. Cavity optomechanics. *Rev. Mod. Phys.* **86**, 1391–1452 (2014). https://doi.org/10.1103/RevModPhys.86.1391.
42. Allan, D. W., Ashby, N. & Hodge, C. C. The science of timekeeping. *Hewlett Packard Application Note 1289* (1997). http://www.allanstime.com/Publications/DWA/Science_Timekeeping/.
43. Wu, N. et al. Hetero-optomechanical crystal zipper cavity for multimode optomechanics. *Photonics* **9**, 78 (2022). https://doi.org/10.3390/photonics9020078.
44. Wu, N. et al. On-chip mechanical exceptional points based on an optomechanical zipper cavity. *Sci. Adv.* **9**, eabp8892 (2023). https://doi.org/10.1126/sciadv.abp8892.
45. Navarro-Urrios, D. et al. Optomechanical crystals for spatial sensing of submicron sized particles. *Sci. Rep.* **11**, 7829 (2021). https://doi.org/10.1038/s41598-021-87558-4.
46. Mercade, L. et al. Floquet phonon lasing in multimode optomechanical systems. *Phys. Rev. Lett.* **127**, 073601 (2021). https://doi.org/10.1103/PhysRevLett.127.073601.

MISCELLANEA

Supplementary materials Supplementary material associated with this article can be found, in the online version, at doi:10.1016/j.chip.2023.100050.

Funding The National Natural Science Foundation of China (Grant No. U22A6004); The National Key Research and Development Program of China (2022YFF1501600, 2018YFB2200402).

Acknowledgments K.C. and F.P. contributed equally to this work. K.C. and F.P. conceived the study. K.C., F.P., and Z.C. performed the theoretical analysis, K.C. and Y.H. supervised the project and advised the device optimization, F.P. and G.B. conducted the sensing experiments, F.P., K.C., and N.W conducted the precision analysis and experiments, F.P. and Z.H conducted the experimental setup. K.C. and F.P. composed the paper, X.F., F.L., W.Z. and Y.H. discussed the results and reviewed the manuscript. The authors would also like to express their sincere gratitudes to the Innovation Center of Advanced Optoelectronic Chip, Institute for Electronics and Information Technology in Tianjin, Tsinghua University for their help with the fabrication of the device.

Data availability Data underlying the results presented in this paper are not publicly available at this time but may be obtained from the authors upon reasonable request.

Declaration of Competing Interest The authors declare no competing interests.